LANGMUIR

pubs.acs.org/Langmuir Article

Molecular Dynamics Study on CO_2 Storage in Water-Filled Kerogen Nanopores in Shale Reservoirs: Effects of Kerogen Maturity and Pore Size

Wenhui Li, Mingshan Zhang, Yiling Nan, Wanying Pang, and Zhehui Jin*

Cite This: https://dx.doi.org/10.1021/acs.langmuir.0c03232 Read Online

ACCESS | Metrics & More | Article Recommendations | Supporting Information

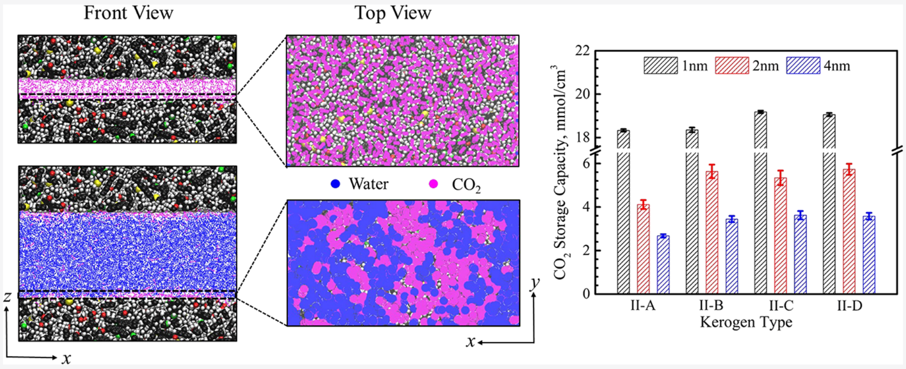

ABSTRACT: CO_2 sequestration in shale reservoirs is an economically viable option to alleviate carbon emission. Kerogen, a major component in the organic matter in shale, is associated with a large number of nanopores, which might be filled with water. However, the CO_2 storage mechanism and capacity in water-filled kerogen nanopores are poorly understood. Therefore, in this work, we use molecular dynamics simulation to study the effects of kerogen maturity and pore size on CO_2 storage mechanism and capacity in water-filled kerogen nanopores. Type II kerogen with different degrees of maturity (II-A, II-B, II-C, and II-D) is chosen, and three pore sizes (1, 2, and 4 nm) are designed. The results show that CO_2 storage mechanisms are different in the 1 nm pore and the larger ones. In 1 nm kerogen pores, water is completely displaced by CO_2 due to the strong interactions between kerogen and CO_2 as well as among CO_2. CO_2 storage capacity in 1 nm pores can be up to 1.5 times its bulk phase in a given volume. On the other hand, in 2 and 4 nm pores, while CO_2 is dissolved in the middle of the pore (away from the kerogen surface), in the vicinity of the kerogen surface, CO_2 can form nano-sized clusters. These CO_2 clusters would enhance the overall CO_2 storage capacity in the nanopores, while the enhancement becomes less significant as pore size increases. Kerogen maturity has minor influences on CO_2 storage capacity. Type II-A (immature) kerogen has the lowest storage capacity because of its high heteroatom surface density, which can form hydrogen bonds with water and reduce the available CO_2 storage space. The other three kerogens are comparable in terms of CO_2 storage capacity. This work should shed some light on CO_2 storage evaluation in shale reservoirs.

1. INTRODUCTION

Since the industrial revolution, the concentration of carbon dioxide (CO_2) in the atmosphere has increased from ~280 ppm to the current level of ~410 ppm.[1] The excessive CO_2 emission has caused serious climate concerns (e.g., global warming).[2,3] To reduce CO_2 content in the atmosphere, CO_2 capture and storage (CCS) in geological underground media becomes vitally important.[2,3] According to the Global Status of CCS (2019),[4] the majority of the sequestrated CO_2 (~30 out of 37 million tonnes per year) is by means of CO_2 enhanced oil recovery (EOR). On the other hand, CO_2-EOR is a promising method for shale exploitation after the primary recovery,[5] and the shale oil/gas production would continue to increase for the next few decades.[6] Therefore, compared with the plain CO_2 geological sequestration, CO_2 stored in shale reservoirs has a huge potential and holds its distinct advantages.[2,3,7] First, from an economic perspective, the enhanced gas/oil production by CO_2 injection can significantly offset the financial burden. In addition, the surface and underground facilities such as wells and pipelines are readily available to reduce the construction cost.[2,3] Second, from a technical perspective, the geological conditions of shale reservoirs have been sufficiently studied.[2,3]

Received: November 8, 2020

Shale reservoirs are typically associated with an organic content from 0.5 wt % to more than 10 wt %.[8] The organic matter (i.e., kerogen) in shale reservoirs contain a considerable number of nano-scale pores.[9−13] Type II kerogen is commonly seen in shale media (such as in Bakken formation and Eagle Ford formation).[5,14] Type II kerogen can be further divided into four sub-types (types II-A, II-B, II-C, and II-D) from low to high maturity as the atomic O/C and H/C ratios decrease.[14−16] On the other hand, during the development of shale reservoirs, there is a massive amount of water existing in the shale formations. The possible water sources include (1) connate water, which typically accounts for 10−30% of the pore volume;[17,18](2) hydraulic fracturing, in which a large amount of water is injected with only a small portion being recovered (e.g., only 7−22% of the injected fluid is recovered in the Marcellus formation[19]); and (3) water alternating gas flooding, in which massive amounts of water is injected into shale formations. While the traditional wisdom is that kerogen is hydrophobic and its hydrophobicity increases as maturity increases,[20,21] a few experimental and simulation studies have shown that water can be trapped in kerogen nanopores even for an over-matured kerogen.[22−24] As a result, it is probable that a considerable number of kerogen nanopores are filled with water.

In water-filled kerogen nanopores, the CO_2 storage mechanism and capacity are still unknown. For example, CO_2 might exist in kerogen nanopores in the dissolved form.[2,3,25] It is observed that gas solubility in the solvent in nanopores differs from that in bulk due to the strong confinement effect.[26] There have been some studies on the gas solubility in the solvent in nano-scale pores.[27−45] They concluded that nano-confinements have significant impacts, either enhancing or reducing the gas solubility in the solvent depending on the confinement properties, pore size, as well as configurations of gas and solvent molecules and their size ratio, and so forth.[26,34,38,42,44,45] The enhanced and reduced gas solubilities are referred to as "over-solubility" and "under-solubility", respectively. The detailed review of the above works can be found in our recent work[44] and a recent review paper.[26] According to our recent works,[44,46] CO_2 solubility in water/brine in the kaolinite and silica nanopores strongly depends on the confinement surface chemistry. Therefore, CO_2 solubility in water in kerogen nanopores might be dependent on its maturity. In addition, Jin and Firoozabadi[47] reported that when the pore size is small, CO_2 can displace water in graphene nanopores which are in chemical equilibrium with an aqueous phase with CO_2 dissolved therein, while in larger pores, CO_2 can only be adsorbed on the hydrophobic pore surface. Therefore, the coordinated effect of kerogen maturity and pore size should be explicitly explored, which determines the CO_2 storage form and capacity in the water-filled kerogen nanopores.

Therefore, in this work, we use molecular dynamics (MD) simulation to study the coordinated effect of kerogen maturity and pore size on CO_2 storage mechanisms and capacity in water-filled kerogen nanopores. MD simulation is applied because it is challenging for experiments to investigate the underlying mechanisms in nanopores at an atomic scale and under high-temperature and high-pressure geological conditions.[48] We use type II kerogen with four different degrees of maturity (types II-A, II-B, II-C, and II-D[14]) associated with three pore sizes (1, 2, and 4 nm) to represent slit-shaped kerogen nanopores. While there have been studies on water and CO_2 adsorption in the kerogen matrix,[49−52]we use slit-shaped kerogen nanopores to study the structural properties of CO_2 and water as such a geometry is one of the most common pore shapes in kerogen.[53] The temperature and pressure are 353 K and 187.2 ± 2.2 bar, respectively, which are the typical shale reservoir conditions.[54,55]

2. METHODS

In this section, we first describe the simulation setup, and then molecular models as well as the simulation details are introduced thereafter.

2.1. Simulation Setup. An example of the simulation setup is shown in Figure 1a. The center of the simulation box has water confined in a slit-shaped kerogen nanopore. On both ends of the pore, in the *x*-direction, two water slabs (serve as outside bulk water reservoirs) and two CO_2 slabs (serve as injected CO_2) are symmetrically placed. The kerogen molecules (types II-A, II-B, II-C, and II-D) are from Ungerer et al.,[14]who developed different kerogen models based on the experimental indexes, such as atomic ratios of H/C and O/C, aromatic carbon fraction, and heteroatom (N, O, and S) content. The procedure of constructing the kerogen matrices can be found in the "Kerogen Matrices Generation" part in the Supporting Information. The final morphology of the inner surfaces of the bottom matrices (see Figure 1a) with their sizes in the *x*−*y* plane is illustrated in Figure 1b. From type II-A to type II-D, the number of aromatic carbons on the pore surface gradually increases, while the number of hydrogen atoms gradually decreases. The morphology of the inner surfaces of the upper matrices (see Figure 1a) as presented in Figure S2 shows a similar phenomenon. The thicknesses of all the bottom and upper kerogen matrices are 2.13 ± 0.03 nm in the *z*-direction. The pore size is denoted as the distance between the innermost atoms on the kerogen inner surfaces in the *z*-direction. Three pore sizes (1, 2, and 4 nm) are designed to represent the kerogen nanopores, which are within the dominant pore size distribution in kerogen.[13,56] CO_2 and water molecules can freely move in the system via molecular diffusion. Once the system reaches equilibrium (chemical potentials of water and CO_2 in the nanopore and bulk water reservoirs are equal[43,44,46]), the distributions of CO_2 and water in the nanopore and bulk water reservoirs can be obtained in the corresponding regions. To minimize the pore end effect, we only use the center region of the

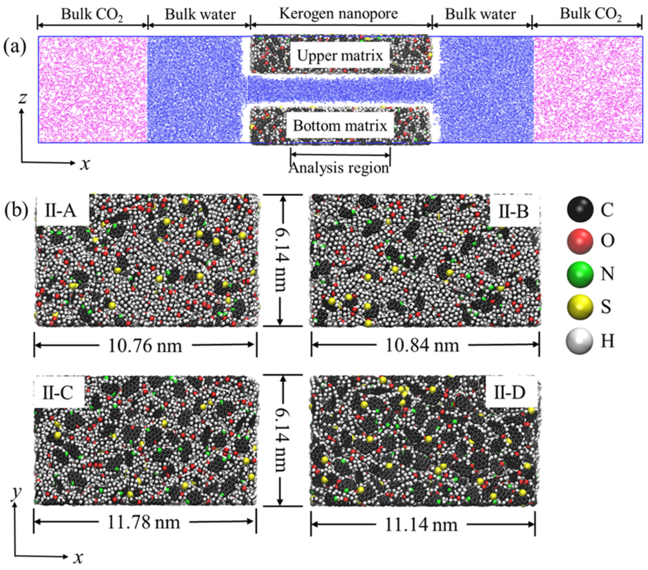

Figure 1. Simulation system setup: (a) initial configuration of the simulation system, taking 2 nm nanopore and type II-A kerogen as an example and (b) morphology of the inner surfaces of the bottom matrices [see (a)] with their sizes in the *x*−*y* plane.

kerogen nanopore (6 nm in the center in the *x*-direction, marked as "analysis region" in Figure 1a) for analysis. The parameters of the system configurations are listed in Table 1. For the 4 nm pore cases, to reduce the computational cost, the thickness of the bulk water reservoirs in the *x*-direction is ~4 nm, which is smaller than that in other cases (~6 nm). It is noted that the ~4 nm water slab is thick enough to obtain the water bulk density and CO_2 solubility in bulk water.

Table 1. Configuration Parameters of All the Simulation Systems[a]

parameter	pore size (nm)	kerogen type II-A	II-B	II-C	II-D
bulk water thickness of each side, nm	1	~6.12	~6.08	~6.11	~5.93
	2	~6.12	~6.08	~6.11	~5.93
	4	~4.12	~4.08	~4.11	~3.93
bulk CO_2 thickness of each side, nm	1	~6.50	~6.50	~6.00	~6.50
	2	~6.50	~6.50	~6.00	~6.50
	4	~6.50	~6.50	~6.00	~6.50
total number of water molecules	1	13,708	13,985	13,993	14,140
	2	18,625	18,625	19,000	18,625
	4	20,000	20,000	20,600	20,000
total number of CO_2 molecules	1	4430	4270	4080	4380
	2	4740	4740	4420	4830
	4	6265	6275	5925	6345
pressure, bar	1	186.8	186.1	185.3	188.3
	2	189.1	187.6	187.2	186.8
	4	187.2	186.1	185.6	185.4

[a] The pressures are obtained by comparing the equilibrated bulk density of CO_2 slab with NIST Chemistry Webbook.[64] The temperature for all the systems is 353 K, and the uncertainties of all the pressures are within ±0.3 bar.

2.2. Molecular Models. Water and CO_2 molecules are simulated by SPC/E[57] and EPM2[58] models, respectively. The Lennard-Jones (LJ) interaction between CO_2 and water molecules are adopted from Vlcek et al.,[59] who optimized the unlike-pair parameters. In our previous works,[44,46] we conducted a thorough validation of water and CO_2 force fields. It has been proven that the optimized SPC/E + EPM2[59] have excellent performances in terms of CO_2 bulk density, CO_2−water interfacial tension, CO_2 solubility in bulk water, and CO_2 diffusion coefficient in bulk water. Therefore, in this work, we use the optimized SPC/E + EPM2[59] to describe water and CO_2. The force field parameters can be found in Table S1 in Supporting Information. The kerogen matrices are described by the consistent valence force field (CVFF).[60] While the original force field used in Ungerer et al.[14] is polymer consistent force field extension (PCFF+), it is difficult to couple with other force fields such as SPC/E and EMP2. This is because PCFF+ uses LJ 9-6 to describe the repulsion and dispersion interactions, while SPC/E and EMP2 use LJ 12-6. On the other hand, CVFF is a good alternative, which has been widely used to model kerogen and its interactions with others (such as CO_2,[24,49,50] water,[24,50] and methane[24,49,50]). To further validate the CVFF force field, we calculate the densities of different kerogen matrices. The simulated densities (unit: g/cm^3) of types II-A, II-B, II-C, and II-D are 1.151 ± 0.003, 1.147 ± 0.003, 1.202 ± 0.002, and 1.359 ± 0.003, respectively, at 353 K and 187 bar (conditions used in this work). Except for type II-B, whose density is not available in the literature, the corresponding experimental densities for types II-A, II-C, and II-D are 1.18−1.29, 1.18−1.25, and 1.30−1.40, respectively.[14] The good agreement between the simulated density and experimental data indicates the validity of the CVFF force field. To test whether water can imbibe into the kerogen nanopores, we set up a number of systems including a kerogen (from immature to over-mature) slit pore and two water slabs on both ends of the pore (see details in the "Water Imbibition into Kerogen Nanopores" part in Supporting Information). We note that water gradually imbibes into all the kerogen nanopores even in 1 nm pores. In addition, we also calculate the water contact angles in the water−vacuum−type II-D kerogen systems (see details in the "Water Contact Angle" part in Supporting Information). The water contact angles on the bottom and upper

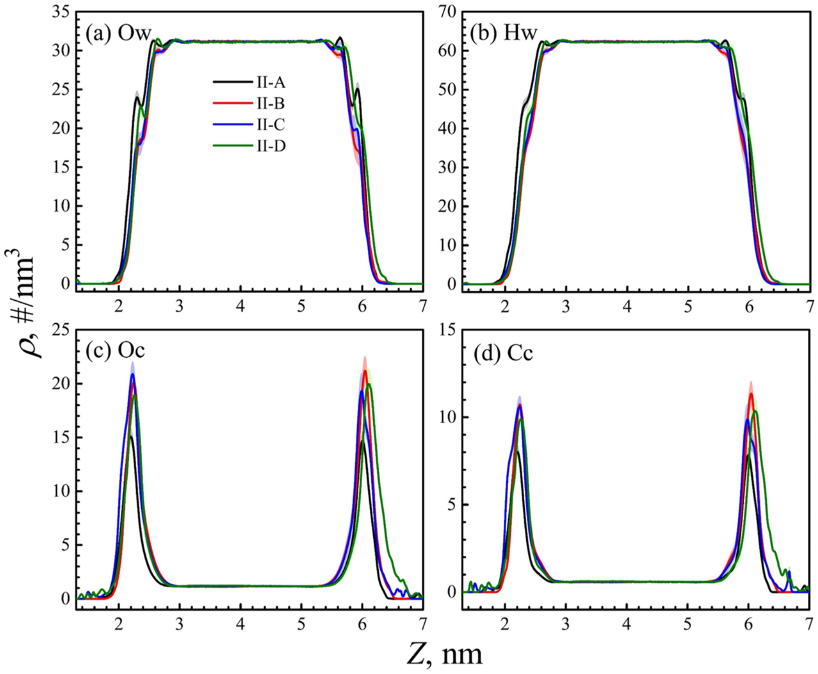

Figure 2. Density profiles of water and CO_2 normal to the kerogen surface in 4 nm slit pores at 353 K and 186.3 ± 1.2 bar. The bands with lighter colors represent the uncertainties of the corresponding density distributions.

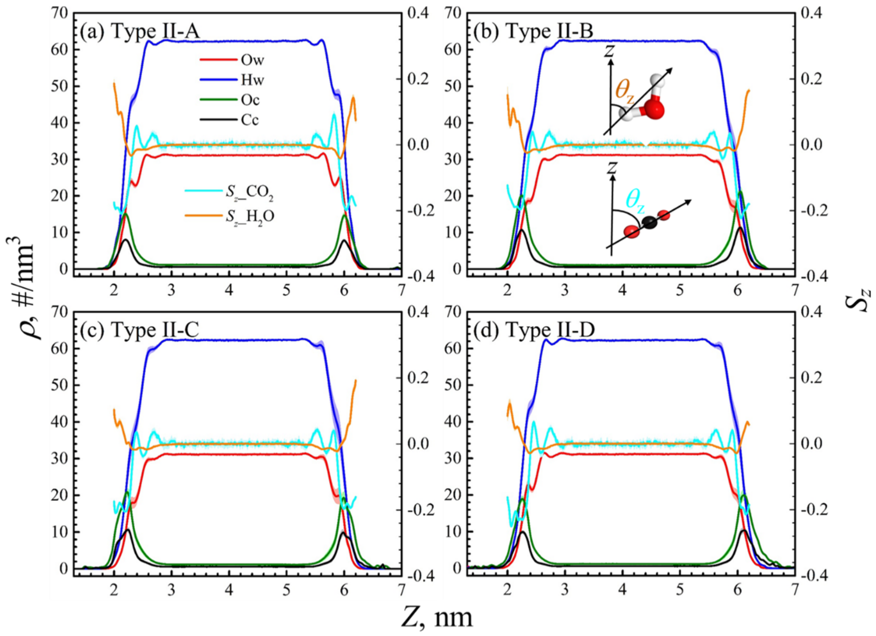

Figure 3. Density profiles and orientation parameters of water and CO_2 normal to the kerogen surfaces in 4 nm slit pores at 353 K and 186.3 ± 1.2 bar. The bands with lighter colors represent the uncertainties of the corresponding distributions.

kerogen surfaces are consistent, which are 43.2 ± 3.2°. Type II-D kerogen shows water-wet properties, which is consistent with the other simulation results[24] and experiments.[22,23] Therefore, we believe that CVFF can faithfully model the kerogen and can be coupled with water and CO_2 with a reasonable accuracy.

2.3. Simulation Details. All the simulation systems are assembled by PACKMOL package[61] and conducted by the GROMACS package (version 2019.5).[62,63] The systems are first relaxed by the steepest descent algorithm until the maximum force on any atom is less than 1000 kJ/(mol·nm), then followed by an *NVT* ensemble simulation with a 2 fs time step for equilibration. The equilibration time for each system varies, which is 200, 90, and 100 ns for the systems with pore size of 1, 2, and 4 nm, respectively. When both water and CO_2 density profiles in the nanopores and outside bulk water reservoirs are stable, we consider that the systems have reached equilibrium. Figures S6 and S7 present an example to determine the equilibrium. Then, a 20 ns *NVT* ensemble simulation for production is followed with a 2 fs time step for each system. The kerogen matrices are always fixed throughout the simulations. The trajectory in the production stage is saved every 200 time steps (400 fs); thus there are total 50,000 frames for data analysis in each system. Three dimensional (3-D) periodic boundary conditions are applied. System pressure is dictated by the density in the bulk CO_2 slabs as shown in Figure 1a from NIST Chemistry Web book[64] as the CO_2 model used can accurately reproduce its density in the studied pressure range.[44,46] The pressure for each system can be found in Table 1, which is in the range of 187.2 ± 2.2 bar. The system temperature is controlled by a velocity rescaling thermostat[65]at 353 K. Except for the interaction between water and CO_2,[59] the LJ interaction between other unlike pairs further than three bonds or in different molecules is calculated by geometric average.[16] LJ potential is truncated at 1.2 nm with tail corrections.[66] The electrostatic interaction is addressed by the particle-mesh Ewald method.[67] Water and CO_2 molecules are rigid, which are achieved by the SETTLE algorithm[68] and by introducing two virtual atoms,[69] respectively.

3. RESULTS AND DISCUSSION

In this section, we first present the kerogen maturity effect on water and CO_2 distributions in 2 and/or 4 nm slit pores and then compare water and CO_2 distributions in type II-B kerogen nanopores with different pore sizes to elaborate the pore size effect. Thereafter, CO_2 storage mechanisms and capacity in kerogen nanopores are discussed.

3.1. Kerogen Maturity Effect. Kerogen maturity effect is illustrated based on density profiles and molecular orientations normal to each kerogen surface, density contour maps parallel to each kerogen surface, and heteroatom and hydrogen bond (H-Bond) distributions on each kerogen surface.

3.1.1. Density Profiles Normal to the Kerogen Surface. Figure 2 depicts the number density distributions of oxygen and hydrogen atoms in water molecules (denoted as Ow and Hw, respectively) and carbon and oxygen atoms in CO_2 molecules (denoted as Cc and Oc, respectively) in 4 nm slit pores normal to the kerogen matrices. The data is extracted from the analysis regions in the slit pores (see Figure 1a) to minimize the pore end effect. Water (Hw and Ow) is generally depleted from the kerogen surface regardless of its maturity, while it is relatively less depleted on type II-A kerogen surfaces compared to others. On the other hand, CO_2 is strongly adsorbed on the kerogen surfaces, forming a prominent adsorption layer on each surface of the pore, in line with previous simulation work.[24] While the CO_2 adsorption amount on the type II-A kerogen surface is relatively small, the adsorption amounts on the other three kerogen surfaces are comparable. Both water and CO_2 densities converge to their respective bulk values in the middle of the pores. In contrast to the pure water density distributions in the 4 nm pores (see Figure S4c), the water adsorption layer on the kerogen surface is displaced by CO_2 when CO_2 is injected. As shown in Figure S6, CO_2 gradually accumulates on the kerogen surface, while water is gradually depleted.

In Figure 3, we present the density profiles of CO_2 and water altogether in various 4 nm kerogen pores. In addition, we also present the orientation parameters of water and CO_2 in Figure 3, which are given as[70−73]

$$S_z = 1.5 \times \langle \cos^2 \theta_z \rangle - 0.5 \quad (1)$$

where S_z represents the orientation parameter of water or CO_2, θ_z is the angle between the z-axis and molecular axis (the lines

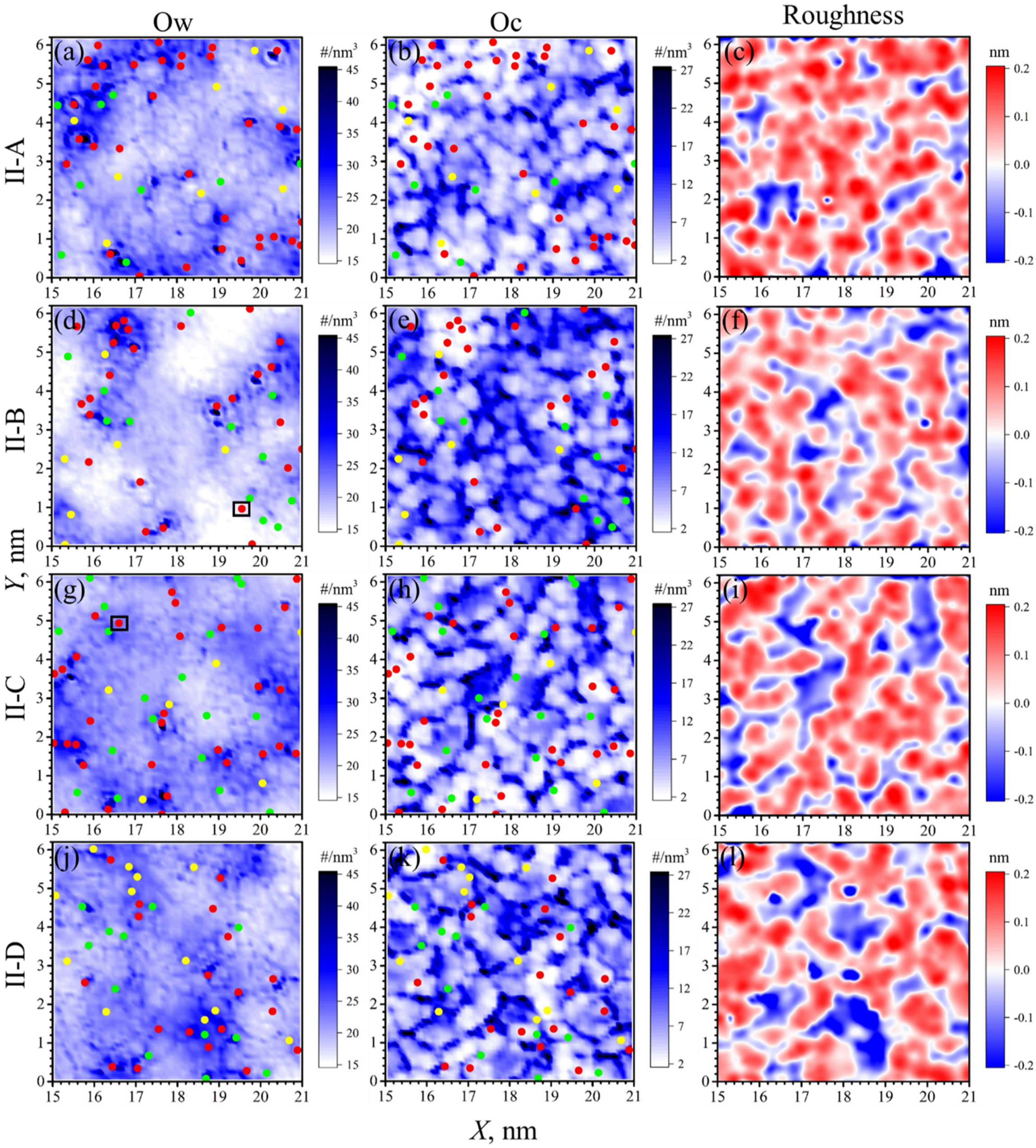

Figure 4. 2-D density contour in the adsorption zone of Ow (first column) and Oc (middle column) parallel to the bottom kerogen surface in 2 nm pores as well as the kerogen surface roughness (third column) in type II-A (first row), type II-B (second row), type II-C (third row), and type II-D (fourth row) kerogen nanopores. The roughness shows the deviation from the average position. Red, green, and yellow circles are the positions of O, N, and S on the kerogen surface, respectively.

connecting two Hw for water and two Oc for CO_2, respectively, as shown in the schematic diagrams in Figure 3b), and $\langle \cdots \rangle$ implies the ensemble average. Positive orientation parameters represent that the molecules are perpendicular to the kerogen surface (fully perpendicular to the surface at $S_z = 1$); negative values mean that the molecules are parallel to the kerogen surface (fully parallel to the surface at $S_z = -0.5$); and $S_z = 0$ indicates a random orientation. We find that CO_2 molecules present a parallel alignment near all the kerogen surfaces, whereas water forms a perpendicular orientation. Both water and CO_2 are randomly distributed in the middle of the pore. The density profiles and orientation parameters in 1 and 2 nm kerogen pores are depicted in Figures S8−S11. The distributions and orientations of water and CO_2 near the kerogen surfaces in 2 nm pores are similar to those in the 4 nm pores, while in the 1 nm pores, CO_2 can completely displace water molecules. Only a negligible number of water molecules exist in the 1 nm pores, while CO_2 can form layering structures. This phenomenon will be further discussed in Section 3.2.

3.1.2. 2-D Density Contour Parallel to Kerogen Surfaces.

To have a better visualization of water and CO_2 distributions near the kerogen surfaces, we depict 2-D density contour plots of Ow and Oc in the adsorption zone parallel to the kerogen surfaces (the $x-y$ plane of 2 nm slit pores) as well as the roughness of the kerogen surfaces in Figure 4. The adsorption zone is defined from the first position where Oc density is 1.1 times of its bulk value (the average density in the middle of the

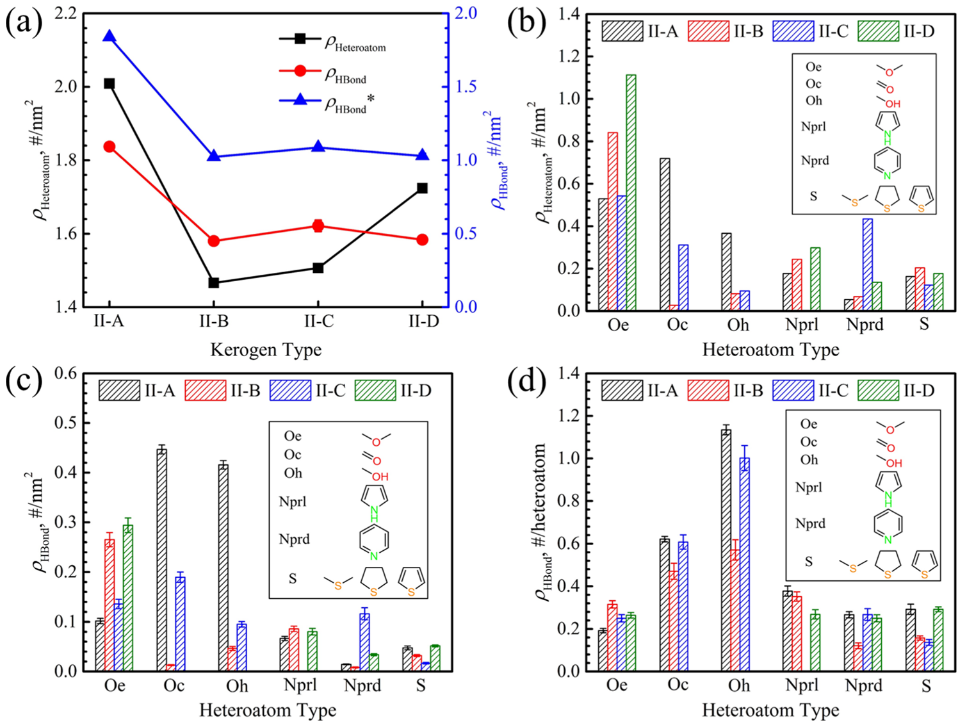

Figure 5. (a) Heteroatom surface density (sum of O, N, and S) as well as H-Bond surface densities between water and heteroatoms in various kerogen nanopores; (b) sorted heteroatom surface densities; (c) H-Bond surface densities between water and sorted heteroatoms; (d) H-Bond densities between water and sorted heteroatom per each heteroatom. $\rho_{\text{H-Bond}}$ means the H-Bond between water and heteroatoms in the systems of H_2O + CO_2 in the kerogen nanopores and $\rho^{*}_{\text{H-Bond}}$ means the H-Bond between water and heteroatoms in the systems of pure H_2O in the kerogen nanopore. All of the results are obtained in 2 nm slit pores.

pore) to the second one in the *z*-direction. The roughness is estimated by the method provided in the study of Düren et al.[74] by rolling a probe particle (with a diameter of 0.2 nm in this work) around the surface of each atom of the kerogen matrix. It shows that in all the kerogen types, water generally accumulates around the heteroatoms (i.e., O, N, and S) at the convex positions, especially O atoms, while it is less densely distributed in the areas where heteroatoms are absent or the concave parts of kerogen surfaces (see the black rectangles highlighted in Figure 4d,g, in which water is less densely distributed while CO_2 accumulates around the O atoms on the concave kerogen surfaces). On the other hand, CO_2 strongly accumulates in the concave parts of kerogen surfaces and weakly accumulates on the convex areas where heteroatoms are absent, while it is generally depleted on the convex areas with the presence of heteroatoms. Overall, the planar CO_2 distribution is mainly dependent on the surface roughness, while that of water is determined by both surface roughness and the presence of heteroatoms. It is also noted that the planar distributions of water and CO_2 in the adsorption zone are similar in 4 nm pores.

3.1.3. Kerogen Surface Property Effect. To further understand the effect of various heteroatoms on water distribution, we present heteroatom surface density (# of heteroatoms per surface area), H-Bond surface densities (# of H-Bond per surface area), and H-Bond formation abilities (# of H-Bond per heteroatom) between water and heteroatoms in 2 nm pores in Figure 5. The heteroatom surface density is obtained by the number of heteroatoms on both bottom and upper surfaces (a thin slab with a thickness of 0.4 nm from the innermost atom of the kerogen toward the kerogen matrix in the *z*-direction. 0.4 nm is chosen as it is close to the diameters of the heteroatoms) in the analysis region (see Figure 1a) divided by the projected area of both the bottom and upper surfaces in the *x*−*y* plane. The H-Bond is determined when the donor−acceptor distance is less than 0.35 nm and the angle between the vectors of donor-H and H-acceptor is less than 30°.[73] As depicted in Figure 5a, type II-A kerogen has the highest heteroatom surface density, followed by type II-D, type II-C, and type II-B. Interestingly, the heteroatom surface density does not monotonically decrease as kerogen maturity increases even though it is believed that the heteroatoms are gradually lost as kerogen evolves from low to high maturity.[21] This is understandable because, from type II-A to type II-D, while the overall trend is that the number of heteroatoms decreases per kerogen molecule (the experimental measurements indicate that the atomic ratios of heteroatoms and carbon for types II-A, II-B, II-C, and II-D are 0.140, 0.091, 0.077, and 0.078, respectively.[14] The above ratios of kerogen models in this work are 0.131, 0.091, 0.083, and 0.085, respectively, which are quite similar to the experimental data), the kerogen molecule becomes smaller (see kerogen molecular formula in Figure S1a). Therefore, to generate a given volume of the kerogen matrix, more kerogen molecules are needed as maturity increases (see "Kerogen Matrices Generation" part in Supporting Information), and the absolute number of heteroatoms in the high maturity kerogen matrices might be larger than that in the low maturity one. Likewise, the heteroatom density on the high maturity kerogen surface might also be higher than that on the low maturity one. In addition, H-Bond surface density between pure water and heteroatoms on type II-A kerogen surface is also the highest (~1.9/nm^2) among the four kerogen types, while those for the other three kerogen types are comparable (~1.0/nm^2). As CO_2 is

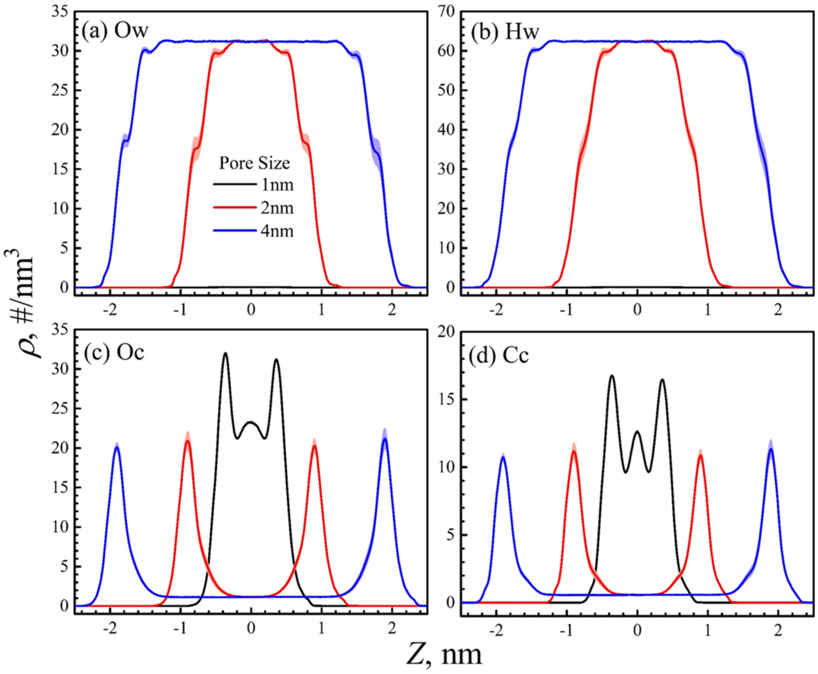

Figure 6. Pore size effect on the density profiles of water and CO_2 in type II-B kerogen nanopores. The horizontal axis is shifted to have all the middle points of the nanopores in the *z*-direction as the origin. The bands with lighter colors represent the uncertainties of the corresponding distributions.

adsorbed on the kerogen surfaces, the H-Bond densities between water and heteroatoms are only half of those when there is no CO_2. In Figure 5b, we sort the O and N atoms into several subgroups according to the functional groups shown in the inset of Figure 5b. The O atoms in ether, carbonyl, and hydroxyl groups are denoted as Oe, Oc, and Oh, respectively; the N atoms in pyrrole and pyridine groups are denoted as Nprl and Nprd, respectively; and S represents all the S atoms including those in sulfide, thiolane, and thiophene groups. Type II-A has the highest O surface density (summation of Oe, Oc, and Oh), especially for Oc and Oh, while type II-D only has Oe, which is the highest among these four kerogen types. In Figure 5c,d, we illustrate the H-Bond surface densities of different types of heteroatoms and the H-Bond number per heteroatom. The results indicate that O atoms (especially Oc and Oh) generally have the highest H-Bond surface density and formation ability. It is also in line with the fact that water tends to accumulate around O atoms on the kerogen surface (see Figure 4). In addition, water on type II-A kerogen surfaces is less depleted compared to others (see Figure 2), because type II-A kerogen with more Oc and Oh on its surfaces can form more H-Bonds than other kerogens.

3.2. Pore Size Effect and CO_2 Storage Mechanisms.

To study the pore size effect, we present water and CO_2 density profiles along the *z*-direction in type II-B kerogen nanopores with various pore sizes in Figure 6. In 2 and 4 nm pores, water and CO_2 have similar distributions: water is depleted from the kerogen surface, where CO_2 is strongly adsorbed. This is also supported by the snapshots depicted in Figure 7b,c. Both water and CO_2 density distributions converge to (pseudo) bulk densities in the middle of the pore, and the molar fraction of CO_2 in the (pseudo) bulk region is identical to that in the outside bulk water reservoirs (see Figure 1a). In addition, the CO_2 and water orientations are random in the (pseudo) bulk region (see Figures 3 and S11). Therefore, the CO_2 distribution in the middle of the pore is governed by the solubility mechanism in which CO_2 is hydrated by water molecules. On the other hand, water and CO_2 molecules near the kerogen surfaces in 2 and 4 nm pores, as depicted in Figure 7e,f, form their respective clusters. The density of CO_2 near the kerogen surface is 1 order of magnitude higher than that in the (pseudo) bulk region in the middle of the pore. A similar result was also observed by the experiment and MD simulation.[75] The non-uniform distribu-

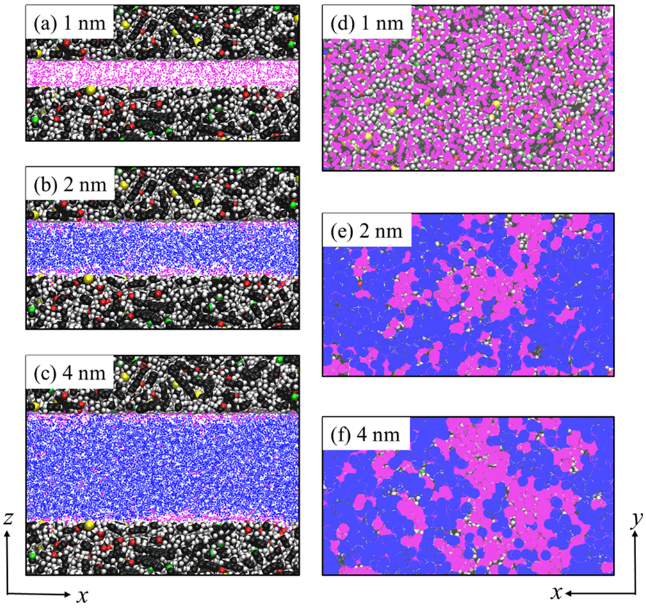

Figure 7. Snapshots of water and CO_2 distribution in type II-B kerogen nanopores with various pore sizes. Panels (a−c) are shown in the *x*−*z* plane and panels (d−f) are shown in the *x*−*y* plane near the kerogen surface. The magenta and blue points represent CO_2 and water, respectively.

tion of water and CO_2 can be attributed to the presence of heteroatoms and surface roughness.[75] On the other hand, in the 1 nm pore, water is initially filled in the nanopores, but it is almost completely displaced by CO_2 after equilibration, and CO_2 can form layering structures as revealed in Figures 6 and 7a,d. A similar phenomenon is also reported by Jin and Firoozabadi,[47] where CO_2 can displace water in 1 nm graphene pores. In small-sized pores, the confinement effect is relatively strong. The strong interactions between kerogen and CO_2 as well as among CO_2 result in a gradual accumulation of CO_2 molecules adsorbed on the kerogen surface and the depletion of water molecules. Thus, CO_2 storage in 1 nm kerogen pore is mainly by adsorption, which is different from that in 2 and 4 nm kerogen pores. The corresponding data for the other types of kerogen can be found in Figures S12−S14, which behave similarly to the type II-B kerogen.

3.3. CO_2 Storage Capacity.

After the discussion of the effect of kerogen maturity and pore size on water and CO_2 distributions and CO_2 storage mechanisms, we evaluate the CO_2 storage capacity S_{cap} in various kerogen nanopores, which is defined as

$$S_{cap} = m_{CO_2}/V_{pore} \tag{2}$$

where m_{CO_2} is the molar number of CO_2 molecules in the analysis region within nanopores (see Figure 1a) and V_{pore} is the effective pore volume obtained from helium uptake method.[44,46] More details can be found in the "Effective Pore Volume" part in the Supporting Information.

In Figure 8, we present CO_2 storage capacity in kerogen nanopores. For comparison, CO_2 solubility in bulk water and CO_2 bulk density under the same conditions (353 K and 187.2 ± 2.2 bar) are given as 0.98 ± 0.02 and 12.76 ± 0.15 mmol/cm^3, respectively. CO_2 solubility in bulk water is obtained from that in the outside bulk water reservoirs (see Figure 1a), which agrees well with experimental data.[76] Type II-A kerogen has the lowest storage capacity among the four types of kerogen due to its high content of heteroatoms on the surface, especially as Oc and Oh which can form strong H-Bonds with water. Thus, more water molecules are trapped in type II-A kerogen pores, while the available pore space for CO_2 is reduced. However, the other three types of kerogen (types II-B, II-C, and II-D) have comparable CO_2 storage capacities. On the other hand, CO_2 storage capacity decreases as pore size increases. Nevertheless, CO_2 storage capacity in the water-filled kerogen nanopores in this work is always higher (at least 1.7 times) than that based on the CO_2 solubility in bulk water. In 1 nm kerogen pores, CO_2 storage capacity is even higher than CO_2 bulk density, reaching up to ∼1.5 times of CO_2 bulk density. These results suggest that the adsorption mechanism renders the highest CO_2 storage capacity, followed by nanoscale CO_2 clusters formed on the kerogen surface.[75] The solubility mechanism in bulk water has the lowest storage capacity in a given volume.

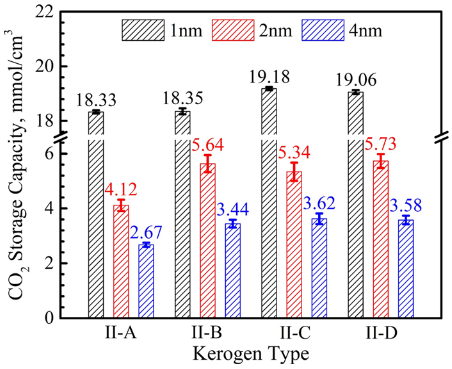

Figure 8. CO_2 storage capacity in all the systems.

4. CONCLUSIONS

In this work, we use MD simulation to study the effects of kerogen maturity and pore size on CO_2 storage mechanism and capacity in water-filled kerogen nanopores. We find that fluid distributions in 1 nm kerogen pores are different from those in larger pores. In the 1 nm kerogen pore, water is completely displaced by CO_2, while CO_2 forms layering structures, due to the strong interactions between kerogen and CO_2 as well as among CO_2. This leads to a high CO_2 storage capacity in the 1 nm kerogen pores, which can be even more than 50% higher than CO_2 bulk density. On the other hand, in the relatively larger pores (2 and 4 nm), CO_2 is stored by the solubility mechanism in the middle of the pore. However, near the kerogen surface, CO_2 and water generally form their respective nano-clusters, due to the presence of heteroatoms and surface roughness. The aggregation of CO_2 molecules on the kerogen surface enhances the overall CO_2 storage capacity in kerogen pores. The increased storage capacity by CO_2 clusters on the surface becomes less significant as pore size increases. The kerogen maturity also imposes a minor influence on CO_2 storage capacity. Type II-A kerogen has a relatively small CO_2 storage capacity compared with others due to its high Oc and Oh contents on its surface, which can form strong H-Bonds with water, thereby reducing the available space for CO_2. The other three types of kerogen (types II-B, II-C, and II-D) have comparable CO_2 storage capacities. This work should provide some important insights into the CO_2 storage evaluation in the shale reservoirs and geological CO_2 sequestrations.

■ ASSOCIATED CONTENT

Supporting Information

The Supporting Information is available free of charge at https://pubs.acs.org/doi/10.1021/acs.langmuir.0c03232.

Kerogen matrices generation; kerogen surface morphology; force field parameters; water imbibition into kerogen nanopores; water contact angle; equilibration check; kerogen maturity effect; pore size effect; and effective pore volume (PDF)

■ AUTHOR INFORMATION

Corresponding Author

Zhehui Jin − *School of Mining and Petroleum Engineering, Department of Civil and Environmental Engineering, University of Alberta, Edmonton, Alberta T6G 1H9, Canada*; orcid.org/0000-0001-8305-5637;
Email: zhehui2@ualberta.ca

Authors

Wenhui Li − *School of Mining and Petroleum Engineering, Department of Civil and Environmental Engineering, University of Alberta, Edmonton, Alberta T6G 1H9, Canada*
Mingshan Zhang − *School of Mining and Petroleum Engineering, Department of Civil and Environmental*

Engineering, University of Alberta, Edmonton, Alberta T6G 1H9, Canada

Yiling Nan − *School of Mining and Petroleum Engineering, Department of Civil and Environmental Engineering, University of Alberta, Edmonton, Alberta T6G 1H9, Canada;* orcid.org/0000-0001-8654-6423

Wanying Pang − *School of Mining and Petroleum Engineering, Department of Civil and Environmental Engineering, University of Alberta, Edmonton, Alberta T6G 1H9, Canada*

Complete contact information is available at: https://pubs.acs.org/10.1021/acs.langmuir.0c03232

Notes

The authors declare no competing financial interest.

■ ACKNOWLEDGMENTS

The authors acknowledge the China Scholarship Council (CSC) for the financial support provided to W.L. and M.Z. This research was enabled in part by support provided by Westgrid (www.westgrid.ca) and Compute Canada (www.computecanada.ca). The authors also greatly acknowledge a Discovery Grant from the Natural Sciences and Engineering Research Council of Canada (NSERC RGPIN-2017-05080). As a part of the University of Alberta's Future Energy Systems research initiative, this research was made possible in part thanks to funding from the Canada First Research Excellence Fund.

■ REFERENCES

(1) World Meteorological Organization. *WMO Statement on the State of the Global Climate in 2019*: Geneva, Switzerland, 2020.

(2) Aminu, M. D.; Nabavi, S. A.; Rochelle, C. A.; Manovic, V. A review of developments in carbon dioxide storage. *Appl. Energy* **2017**, *208*, 1389−1419.

(3) Bui, M.; Adjiman, C. S.; Bardow, A.; Anthony, E. J.; Boston, A.; Brown, S.; Fennell, P. S.; Fuss, S.; Galindo, A.; Hackett, L. A.; Hallett, J. P.; Herzog, H. J.; Jackson, G.; Kemper, J.; Krevor, S.; Maitland, G. C.; Matuszewski, M.; Metcalfe, I. S.; Petit, C.; Puxty, G.; Reimer, J.; Reiner, D. M.; Rubin, E. S.; Scott, S. A.; Shah, N.; Smit, B.; Trusler, J. P. M.; Webley, P.; Wilcox, J.; Mac Dowell, N. Carbon capture and storage (CCS): the way forward. *Energy Environ. Sci.* **2018**, *11*, 1062−1176.

(4) Global CCS Institute. *The Global Status of CCS: 2019. Targeting Climate Change*, 2019.

(5) Jia, B.; Tsau, J.-S.; Barati, R. A review of the current progress of CO2 injection EOR and carbon storage in shale oil reservoirs. *Fuel* **2019**, *236*, 404−427.

(6) US Energy Information Administration. *Annual Energy Outlook 2019*, 2019.

(7) Zhang, M.; Zhan, S.; Jin, Z. Recovery mechanisms of hydrocarbon mixtures in organic and inorganic nanopores during pressure drawdown and CO2 injection from molecular perspectives. *Chem. Eng. J.* **2020**, *382*, 122808.

(8) Shi, Y.; Yassin, M. R.; Yuan, L.; Dehghanpour, H. Modelling imbibition data for determining size distribution of organic and inorganic pores in unconventional rocks. *Int. J. Coal Geol.* **2019**, *201*, 26−43.

(9) Jin, Z.; Firoozabadi, A. Thermodynamic modeling of phase behavior in shale media. *SPE J.* **2016**, *21*, 190−207.

(10) Pang, W.; He, Y.; Yan, C.; Jin, Z. Tackling the challenges in the estimation of methane absolute adsorption in kerogen nanoporous media from molecular and analytical approaches. *Fuel* **2019**, *242*, 687−698.

(11) Zhan, S.; Su, Y.; Jin, Z.; Wang, W.; Li, L. Effect of water film on oil flow in quartz nanopores from molecular perspectives. *Fuel* **2020**, *262*, 116560.

(12) Lau, H. C.; Radhamani, A. V.; Ramakrishna, S. Maximizing Production from Shale Reservoir by Using Micro-Sized Proppants. *International Petroleum Technology Conference*; International Petroleum Technology Conference, 2019.

(13) Kuila, U.; Prasad, M. Specific surface area and pore-size distribution in clays and shales. *Geophys. Prospect.* **2013**, *61*, 341−362.

(14) Ungerer, P.; Collell, J.; Yiannourakou, M. Molecular modeling of the volumetric and thermodynamic properties of kerogen: Influence of organic type and maturity. *Energy Fuels* **2015**, *29*, 91−105.

(15) Behar, F.; Vandenbroucke, M. Chemical modelling of kerogens. *Org. Geochem.* **1987**, *11*, 15−24.

(16) Sun, Z.; Li, X.; Liu, W.; Zhang, T.; He, M.; Nasrabadi, H. Molecular dynamics of methane flow behavior through realistic organic nanopores under geologic shale condition: Pore size and kerogen types. *Chem. Eng. J.* **2020**, *398*, 124341.

(17) Gao, Z.; Hu, Q. Initial water saturation and imbibition fluid affect spontaneous imbibition into Barnett shale samples. *J. Nat. Gas Sci. Eng.* **2016**, *34*, 541−551.

(18) Tao, Z.; Bielicki, J. M.; Clarens, A. F. Physicochemical factors impacting CO2 sequestration in depleted shale formations: The case of the Utica shale. *Energy Procedia* **2014**, *63*, 5153−5163.

(19) Balashov, V. N.; Engelder, T.; Gu, X.; Fantle, M. S.; Brantley, S. L. A model describing flowback chemistry changes with time after Marcellus Shale hydraulic fracturingMarcellus Shale Hydraulic Fracturing. *AAPG Bull.* **2015**, *99*, 143−154.

(20) Jagadisan, A.; Heidari, Z. Experimental Quantification of the Effect of Thermal Maturity of Kerogen on Its Wettability. *SPE Reservoir Eval. Eng.* **2019**, *22*, 1323.

(21) Hu, Y.; Devegowda, D.; Sigal, R. A microscopic characterization of wettability in shale kerogen with varying maturity levels. *J. Nat. Gas Sci. Eng.* **2016**, *33*, 1078−1086.

(22) Ruppert, L. F.; Sakurovs, R.; Blach, T. P.; He, L.; Melnichenko, Y. B.; Mildner, D. F. R.; Alcantar-Lopez, L. A USANS/SANS study of the accessibility of pores in the Barnett Shale to methane and water. *Energy Fuels* **2013**, *27*, 772−779.

(23) Gu, X.; Mildner, D. F. R.; Cole, D. R.; Rother, G.; Slingerland, R.; Brantley, S. L. Quantification of organic porosity and water accessibility in Marcellus shale using neutron scattering. *Energy Fuels* **2016**, *30*, 4438−4449.

(24) Ho, T. A.; Wang, Y.; Ilgen, A.; Criscenti, L. J.; Tenney, C. M. Supercritical CO2-induced atomistic lubrication for water flow in a rough hydrophilic nanochannel. *Nanoscale* **2018**, *10*, 19957−19963.

(25) Yan, W.; Huang, S.; Stenby, E. H. Measurement and modeling of CO2 solubility in NaCl brine and CO2−saturated NaCl brine density. *Int. J. Greenhouse Gas Control* **2011**, *5*, 1460−1477.

(26) Coasne, B.; Farrusseng, D. Gas oversolubility in nanoconfined liquids: Review and perspectives for adsorbent design. *Microporous Mesoporous Mater.* **2019**, *288*, 109561.

(27) Luzar, A.; Bratko, D. Gas solubility in hydrophobic confinement. *J. Phys. Chem. B* **2005**, *109*, 22545−22552.

(28) Bratko, D.; Luzar, A. Attractive surface force in the presence of dissolved gas: A molecular approach. *Langmuir* **2008**, *24*, 1247−1253.

(29) Qiao, Y.; Cao, G.; Chen, X. Effects of gas molecules on nanofluidic behaviors. *J. Am. Chem. Soc.* **2007**, *129*, 2355−2359.

(30) Miachon, S.; Syakaev, V. V.; Rakhmatullin, A.; Pera-Titus, M.; Caldarelli, S.; Dalmon, J.-A. Higher gas solubility in nanoliquids? *ChemPhysChem* **2008**, *9*, 78−82.

(31) Pera-Titus, M.; Miachon, S.; Dalmon, J. A. Increased gas solubility in nanoliquids: Improved performance in interfacial catalytic membrane contactors. *AlChE J.* **2009**, *55*, 434−441.

(32) Rakotovao, V.; Ammar, R.; Miachon, S.; Pera-Titus, M. Influence of the mesoconfining solid on gas oversolubility in nanoliquids. *Chem. Phys. Lett.* **2010**, *485*, 299−303.

(33) Ho, N. L.; Porcheron, F.; Pellenq, R. J.-M. Experimental and molecular simulation investigation of enhanced CO2 solubility in hybrid adsorbents. *Langmuir* **2010**, *26*, 13287−13296.

(34) Ho, L. N.; Perez Pellitero, J.; Porcheron, F.; Pellenq, R. J.-M. Enhanced CO2 solubility in hybrid MCM-41: molecular simulations and experiments. *Langmuir* **2011**, *27*, 8187−8197.

(35) Ho, N. L.; Perez-Pellitero, J.; Porcheron, F.; Pellenq, R. J.-M. Enhanced CO2 solubility in hybrid adsorbents: optimization of solid support and solvent properties for CO2 capture. *J. Phys. Chem. C* **2012**, *116*, 3600−3607.

(36) Clauzier, S.; Ho, L. N.; Pera-Titus, M.; Coasne, B.; Farrusseng, D. Enhanced H2 uptake in solvents confined in mesoporous metal−organic framework. *J. Am. Chem. Soc.* **2012**, *134*, 17369−17371.

(37) Soubeyrand-Lenoir, E.; Vagner, C.; Yoon, J. W.; Bazin, P.; Ragon, F.; Hwang, Y. K.; Serre, C.; Chang, J.-S.; Llewellyn, P. L. How water fosters a remarkable 5-fold increase in low-pressure CO2 uptake within mesoporous MIL-100 (Fe). *J. Am. Chem. Soc.* **2012**, *134*, 10174−10181.

(38) Ho, L. N.; Clauzier, S.; Schuurman, Y.; Farrusseng, D.; Coasne, B. Gas uptake in solvents confined in mesopores: adsorption versus enhanced solubility. *J. Phys. Chem. Lett.* **2013**, *4*, 2274−2278.

(39) Phan, A.; Cole, D. R.; Striolo, A. Aqueous methane in slit-shaped silica nanopores: high solubility and traces of hydrates. *J. Phys. Chem. C* **2014**, *118*, 4860−4868.

(40) Ho, L. N.; Schuurman, Y.; Farrusseng, D.; Coasne, B. Solubility of gases in water confined in nanoporous materials: ZSM-5, MCM-41, and MIL-100. *J. Phys. Chem. C* **2015**, *119*, 21547−21554.

(41) Hu, Y.; Huang, L.; Zhao, S.; Liu, H.; Gubbins, K. E. Effect of confinement in nano-porous materials on the solubility of a supercritical gas. *Mol. Phys.* **2016**, *114*, 3294−3306.

(42) Gadikota, G.; Dazas, B.; Rother, G.; Cheshire, M. C.; Bourg, I. C. Hydrophobic solvation of gases (CO2, CH4, H2, noble gases) in clay interlayer nanopores. *J. Phys. Chem. C* **2017**, *121*, 26539−26550.

(43) Badmos, S. B.; Striolo, A.; Cole, D. R. Aqueous Hydrogen Sulfide in Slit-Shaped Silica Nanopores: Confinement Effects on Solubility, Structural, and Dynamical Properties. *J. Phys. Chem. C* **2018**, *122*, 14744−14755.

(44) Li, W.; Nan, Y.; Zhang, Z.; You, Q.; Jin, Z. Hydrophilicity/Hydrophobicity Driven CO2 Solubility in Kaolinite Nanopores in Relation to Carbon Sequestration. *Chem. Eng. J.* **2020**, *398*, 125449.

(45) Qiao, C.; Yu, X.; Song, X.; Zhao, T.; Xu, X.; Zhao, S.; Gubbins, K. E. Enhancing Gas Solubility in Nanopores: A Combined Study Using Classical Density Functional Theory and Machine Learning. *Langmuir* **2020**, *36*, 8527−8536.

(46) Li, W.; Nan, Y.; You, Q.; Jin, Z. CO2 Solubility in Brine in Silica Nanopores in Relation to Geological CO2 Sequestration in Tight Formations: Effect of Salinity and pH. *Chem. Eng. J.* **2020**, 127626.

(47) Jin, Z.; Firoozabadi, A. Phase behavior and flow in shale nanopores from molecular simulations. *Fluid Phase Equilib.* **2016**, *430*, 156−168.

(48) Gilfillan, S. M. V.; Lollar, B. S.; Holland, G.; Blagburn, D.; Stevens, S.; Schoell, M.; Cassidy, M.; Ding, Z.; Zhou, Z.; Lacrampe-Couloume, G.; Ballentine, C. J. Solubility trapping in formation water as dominant CO 2 sink in natural gas fields. *Nature* **2009**, *458*, 614−618.

(49) Michalec, L.; Lísal, M. Molecular simulation of shale gas adsorption onto overmature type II model kerogen with control microporosity. *Mol. Phys.* **2017**, *115*, 1086−1103.

(50) Chong, L.; Sanguinito, S.; Goodman, A. L.; Myshakin, E. M. Molecular characterization of carbon dioxide, methane, and water adsorption in micropore space of kerogen matrix. *Fuel* **2021**, *283*, 119254.

(51) Sui, H.; Zhang, F.; Wang, Z.; Wang, D.; Wang, Y. Effect of Kerogen Maturity, Water Content for Carbon Dioxide, Methane, and Their Mixture Adsorption and Diffusion in Kerogen: A Computational Investigation. *Langmuir* **2020**, *36*, 9756−9769.

(52) Tesson, S.; Firoozabadi, A. Deformation and Swelling of Kerogen Matrix in Light Hydrocarbons and Carbon Dioxide. *J. Phys. Chem. C* **2019**, *123*, 29173−29183.

(53) Song, W.; Yao, J.; Ma, J.; Li, A.; Li, Y.; Sun, H.; Zhang, L. Grand canonical Monte Carlo simulations of pore structure influence on methane adsorption in micro-porous carbons with applications to coal and shale systems. *Fuel* **2018**, *215*, 196−203.

(54) Curtis, J. B. Fractured shale-gas systems. *AAPG Bull.* **2002**, *86*, 1921−1938.

(55) Nan, Y.; Li, W.; Jin, Z. Slip length of methane flow under shale reservoir conditions: Effect of pore size and pressure. *Fuel* **2020**, *259*, 116237.

(56) Chalmers, G. R.; Bustin, R. M.; Power, I. M. Characterization of gas shale pore systems by porosimetry, pycnometry, surface area, and field emission scanning electron microscopy/transmission electron microscopy image analyses: Examples from the Barnett, Woodford, Haynesville, Marcellus, and Doig unitsCharacterization of Gas Shale Pore Systems. *AAPG Bull.* **2012**, *96*, 1099−1119.

(57) Berendsen, H. J. C.; Grigera, J. R.; Straatsma, T. P. The missing term in effective pair potentials. *J. Phys. Chem.* **1987**, *91*, 6269−6271.

(58) Harris, J. G.; Yung, K. H. Carbon dioxide's liquid-vapor coexistence curve and critical properties as predicted by a simple molecular model. *J. Phys. Chem.* **1995**, *99*, 12021−12024.

(59) Vlcek, L.; Chialvo, A. A.; Cole, D. R. Optimized unlike-pair interactions for water−carbon dioxide mixtures described by the SPC/E and EPM2 models. *J. Phys. Chem. B* **2011**, *115*, 8775−8784.

(60) Hagler, A. T.; Lifson, S.; Dauber, P. Consistent force field studies of intermolecular forces in hydrogen-bonded crystals. 2. A benchmark for the objective comparison of alternative force fields. *J. Am. Chem. Soc.* **1979**, *101*, 5122−5130.

(61) Martínez, L.; Andrade, R.; Birgin, E. G.; Martínez, J. M. PACKMOL: a package for building initial configurations for molecular dynamics simulations. *J. Comput. Chem.* **2009**, *30*, 2157−2164.

(62) Berendsen, H. J. C.; van der Spoel, D.; van Drunen, R. GROMACS: a message-passing parallel molecular dynamics implementation. *Comput. Phys. Commun.* **1995**, *91*, 43−56.

(63) Van Der Spoel, D.; Lindahl, E.; Hess, B.; Groenhof, G.; Mark, A. E.; Berendsen, H. J. C. GROMACS: fast, flexible, and free. *J. Comput. Chem.* **2005**, *26*, 1701−1718.

(64) Lemmon, E. W.; McLinden, M. O.; Friend, D. G. Thermophysical Properties of Fluid Systems. In *NIST Chemistry WebBook, NIST Standard Reference Database Number 69*; Linstrom, P. J.; Mallard, W. G., Eds.; National Institute of Standards and Technology: Gaithersburg MD, 2020.

(65) Bussi, G.; Donadio, D.; Parrinello, M. Canonical sampling through velocity rescaling. *J. Chem. Phys.* **2007**, *126*, 014101.

(66) Allen, M.; Tildesley, D. J. *Computer Simulation of Liquids*; Clarendon Press: Oxford, 1987.

(67) Essmann, U.; Perera, L.; Berkowitz, M. L.; Darden, T.; Lee, H.; Pedersen, L. G. A smooth particle mesh Ewald method. *J. Chem. Phys.* **1995**, *103*, 8577−8593.

(68) Miyamoto, S.; Kollman, P. A. Settle: An analytical version of the SHAKE and RATTLE algorithm for rigid water models. *J. Comput. Chem.* **1992**, *13*, 952−962.

(69) Berendsen, H.; Van Gunsteren, W. Molecular dynamics simulations: Techniques and approaches. *Molecular Liquids*; Springer, 1984; pp 475−500.

(70) Yang, X.; Zhang, C. Structure and diffusion behavior of dense carbon dioxide fluid in clay-like slit pores by molecular dynamics simulation. *Chem. Phys. Lett.* **2005**, *407*, 427−432.

(71) Singh, S. K.; Sinha, A.; Deo, G.; Singh, J. K. Vapor− liquid phase coexistence, critical properties, and surface tension of confined alkanes. *J. Phys. Chem. C* **2009**, *113*, 7170−7180.

(72) Jin, Z.; Firoozabadi, A. Methane and carbon dioxide adsorption in clay-like slit pores by Monte Carlo simulations. *Fluid Phase Equilib.* **2013**, *360*, 456−465.

(73) Li, W.; Nan, Y.; Wen, X.; Wang, W.; Jin, Z. Effects of Salinity and N-, S-, and O-Bearing Polar Components on Light Oil-Brine Interfacial Properties from Molecular Perspectives. *J. Phys. Chem. C* **2019**, *123*, 23520−23528.

(74) Düren, T.; Millange, F.; Férey, G.; Walton, K. S.; Snurr, R. Q. Calculating geometric surface areas as a characterization tool for

metal– organic frameworks. *J. Phys. Chem. C* **2007**, *111*, 15350–15356.

(75) Zhou, L.; Wang, X.; Shin, H.-J.; Wang, J.; Tai, R.; Zhang, X.; Fang, H.; Xiao, W.; Wang, L.; Wang, C.; Gao, X.; Hu, J.; Zhang, L. Ultrahigh Density of Gas Molecules Confined in Surface Nanobubbles in Ambient Water. *J. Am. Chem. Soc.* **2020**, *142*, 5583–5593.

(76) Spycher, N.; Pruess, K. CO2-H2O Mixtures in the Geological Sequestration of CO2. II. Partitioning in Chloride Brines at 12–100 C and up to 600 bar. *Geochim. Cosmochim. Acta* **2005**, *69*, 3309–3320.